Journal of Advanced Research in Fluid Mechanics and Thermal Sciences

Journal homepage:
https://semarakilmu.com.my/journals/index.php/fluid_mechanics_thermal_sciences/index
ISSN: 2289-7879

CFD Impingement Flow Study on Temperature Profile of Concave Plate

Hamdan Abdul Hamid[1], Wong Kuk Yong[1], Hamid Yusoff[2], Mohd Azmi Ismail[1,*]

[1] School of Mechanical Engineering, Universiti Sains Malaysia, 14300 Nibong Tebal, Pulau Pinang, Malaysia
[2] Advanced Mechanics Research Group, Faculty of Mechanical Engineering, Universiti Teknologi MARA, Cawangan Pulau Pinang, 13500 Permatang Pauh, Pulau Pinang, Malaysia

ARTICLE INFO

Article history:
Received 15 January 2022
Received in revised form 3 April 2022
Accepted 7 April 2022
Available online 2 May 2022

Keywords:
CFD; anti-icing; temperature

ABSTRACT

All the aircraft are equipped with an anti-icing system to prevent ice accretion on the body of the aircraft. The anti-icing system is important because ice accretion degrades the performance of the aircraft and may cause aircraft crashes. Piccolo tube Anti-icing system uses the impingement hot air and creates hotspot on nacelle lip-skin and edges of wings. The temperature distribution caused by the impingement of hot air must be studied to get a better design of the anti-icing system. The skin geometry shape affects hot airflow behavior in the impingement vicinity, hence influences temperature distribution on wing skin and nacelle lip-skin. Thus, the CFD simulation of the hot air impingement air various concave curvature radius was conducted by using ANSYS Fluent 19.2. The result shows the temperature contour has been plotted from the software. Correlation between Nusselt number on impingement point and Reynolds number was successfully done as the validation. Increasing the Reynolds number increases the dimensionless temperature of the concave plate. Temperature is 0.147125 has been recorded as the highest dimensionless temperature under the set of an air temperature of 43°C, Reynolds number of 4070, and 300mm curvature radius. Besides that, increases in heat dissipation decrease the dimensionless temperature of the plate with the curvature radius also decreases. The dimensionless temperature increases from 0.138747 to 0.142316 when the curvature radius increases from 150mm to 300mm.

1. Introduction

Aviation fatalities is a disaster and one of the common causes of air accident is an icing [1]. In-flight and in-taxi conditions, icing can lead to serious trouble for the aircraft. Icing also can cause stall and loss of control which impact is very dangerous to the passengers. De-icing and anti-icing systems are equipped at all aircraft to overcome the icing problem. Both of these systems use different energy to remove the ice including mechanical, chemical, and thermal energy. Pneumatic inflatable boot (PIB) [2], Electro Impulse De-icing (EIDI) [3], and Electro-Magnetic Expulsion De-icing (EMEDS) [4] utilize mechanical energy while chemical Fluid Anti Icing (FAI) [5] is used when weeping wing to remove the ice accretion. Piccolo Tube Anti Icing (PTAI) [6] and Swirl Anti Icing (SAI) [7] system utilize thermal energy to prevent the formation of ice. The phenomenon that ice accretion occurs on the

* *Corresponding author.*
E-mail address: azmi_meche@usm.my

https://doi.org/10.37934/arfmts.95.1.116

surfaces of aircraft is aircraft icing. It is a serious threat to flight safety. The ice is formed when supercooled water droplets in the clouds impinge on aircraft [8]. Some important parts of aircraft such as leading edges of the wing, tails, engine inlet, windshield, and helicopter blade icing usually occur [9]. Ice accretion can degrade the performance of aircraft as it causes an increase of weight and drag, reduction of lift and thrust. During take-off, the clear ice loosened and was ingested by the engines. Engines failure could have happened because the ice will damage the engine fan stages and caused engine surges. If the condition is critical, an air crash may happen due to icing.

There are two types of ice protection systems mostly equipped in commercial aviation namely, the anti-icing system (AI) and de-icing system (DI). Anti-icing systems are pre-emptive systems, they are activated before the flight enters icing conditions. Anti-icing systems are aimed to prevent ice from forming by providing energy continuously. De-icing systems are used to periodically get rid of accreted ice when the ice has accumulated to a significant thickness [10]. Piccolo Tube Anti-Icing system (PTAI) is one of the famous hot-air anti-icing systems. Tube with a series of in-line or staggered holes placed inside the wing leading end near to its inner surface. The hot air is blown out from the engine compressor, is then passed through the piccolo tube. The hot air is ejected from the piccolo tube holes at high velocity and impinges on the inner surface of the wing leading edge. Hot enough to prevent ice accretion heat is conducted from the wing inner surface to the outer surface so that the outer surface of the wing leading edge [11]. Swirl Anti-Icing (SAI) system, the air with high temperature and velocity exits from the nozzle and mixes with the cool stationary air in the D-chamber, which causes a large amount of cold air entrained by hot air. Hot air from the jet engine is directed to the D-chamber at high pressure by a supply pipe. The end of the nozzle is bent 90° so that the hot air can be expelled at a high velocity substantially along a tangent to the middle circle of the D-chamber. Eventually, the mixed air swirls circularly around the annular D-chamber [1].

Ice accretion can be happened either on the ground or in the air. Slush, snow, clear ice, or a combination of them were caused by the snow on the ground situation. Icing commonly happens in-flight during the take-off or landing phase of a flight, when the aircraft needs to fly through clouds in which the temperatures are at or below freezing point [12]. The droplets may be swept off from the surface by aerodynamic forces or freeze [13]. Ice accretion has four types in-flight leading-edge ice accretions, runback and “ridge” ice accretions, large in-flight and ground frost/ice accretions causes maximum lift reductions, the corresponding stall angle reductions, resulting in drag penalties, and trailing-edge control surface anomalies. Lynch and Khodadoust [14] have addressed the aerodynamic performance and control degradations caused by various types of ice accretions on the lifting surfaces of fixed-wing aircraft. The parting strip located near the stagnation point can greatly prevent ice from covering the entire leading edge. At the upper and lower segment, the ice will be accumulated. Eliminating the ice bridge formed at the stagnation point, ice shedding efficiency increases. This separation leads to greater aerodynamic forces on the ice. Hann *et al.,* [15] have identified the most energy-efficient ice protection system (IPS) method among anti-icing systems, conventional de-icing systems, and de-icing with the parting strip. A parting strip (PS) is a special heating zone that is constantly heated and can be used to minimize the energy needed for de-icing [16]. The most efficient system De-icing has proven to require much lower heat loads at all temperatures. A conventional IPS, with a periodically heated leading-edge, and a parting strip IPS, with a continuously heated small area, were tested for de-icing. De-icing with the parting strip needs 50% less energy than a conventional de-icing system.

In some simulation or CFD study of impingement heat transfer, Seyedein *et al.,* [17] have modelled a single confined turbulent slot jet impingement using various isotropic two-equation k-ε turbulence models. The standard k-ε turbulence model is not the most suitable model to simulate the confined turbulent impinging jet. The accuracy of the results is greatly affected by the model

parameters and the near-wall treatment. Low-Reynolds versions of the k-ε model are suitable for modelling turbulent impinging jets. Shi *et al.,* [18] used commercial finite volume code FLUENT 5.0 to simulate the heat transfer characteristics of a single impinging semiconfined slot jet under turbulence models, near-wall treatments, turbulence intensity, jet Reynolds number, and the type of thermal boundary condition on the heat transfer by using standard k-ε and RSM models. Both the models marginally overpredicted the Nusselt number distributions under some conditions.

In fact, the CFD impingement study not only applied for aircraft anti-icing only. Some researchers employed a CFD impingement study for the cooling system. For example, Azmi *et al.,* [19] employed a synthetic jet to enhance heat impingement heat transfer coefficient. Another example, Ismail *et al.,* [20] used high frequency and low amplitude of synthetic jet impingement to reduces the temperature of the electronic component. Most recently, the impingement study was applied on stagnation point together with non-linear thermal radiation [21].

The simulated results performed well for large nozzle-to-target spacing if compared to the experimental results, but the predictions for small nozzle-to-target spacing are inadequate in the concave plate. The objective is to conduct CFD simulation at various Reynolds numbers of impingement flow, hot air temperature, and concave radius on concave plate. Thus, the temperature distribution of the concave plate is investigated and discussed in the present study.

2. Methodology

The model and dimension, the boundary condition, and the computational setup are discussed in this section.

2.1 Geometric Modelling and Dimensions

The geometry is divided into three parts nozzle, air, and concave plate. The modelling of geometry was developed using the software Solid works 2020. The nozzle is 20mm long with a diameter of 2.5mm. The length and width of the concave plate are fixed at 100mm with different radius of the concave. The curvature radii of the concave plate are 150mm, 200mm, 250mm, and 300mm. Air is the part between the nozzle and the concave plate. The distance between the nozzle outlet and the plate is 37.5mm which is 15 times of nozzle diameter. The geometry was drawn as shown in Figure 1, Figure 2 and Figure 3.

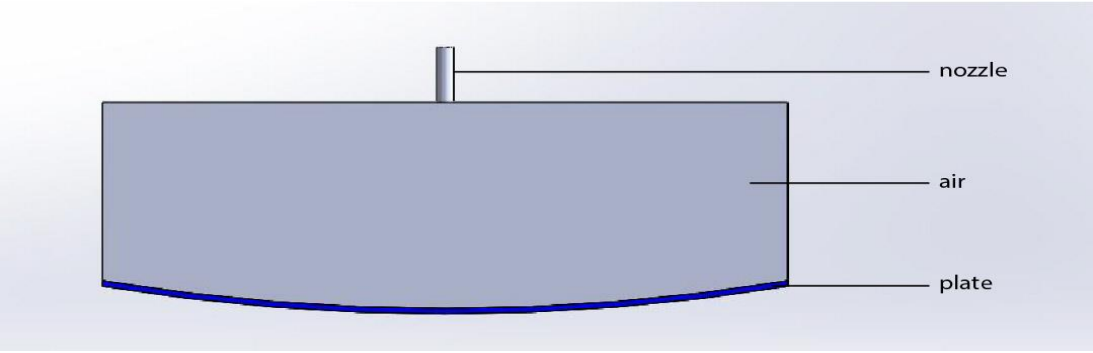

Fig. 1. The geometry of the concave plate

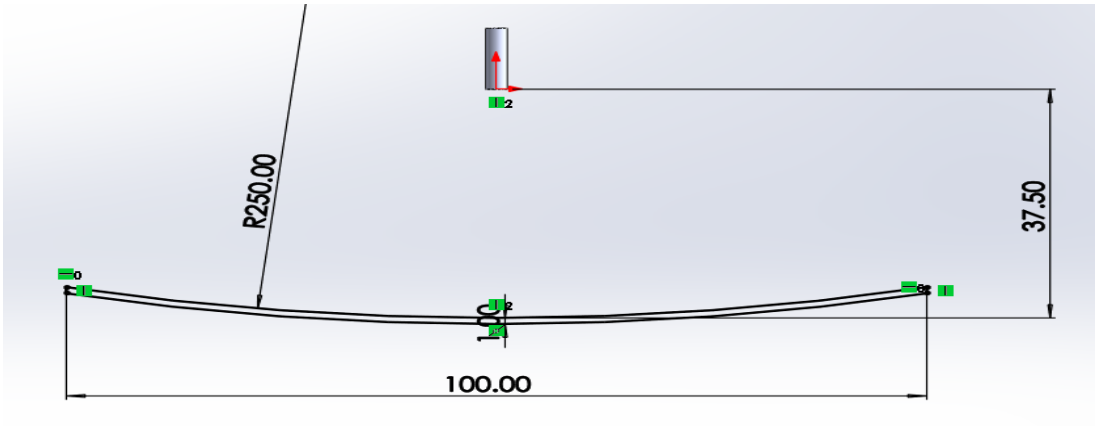

Fig. 2. Dimension of the geometry

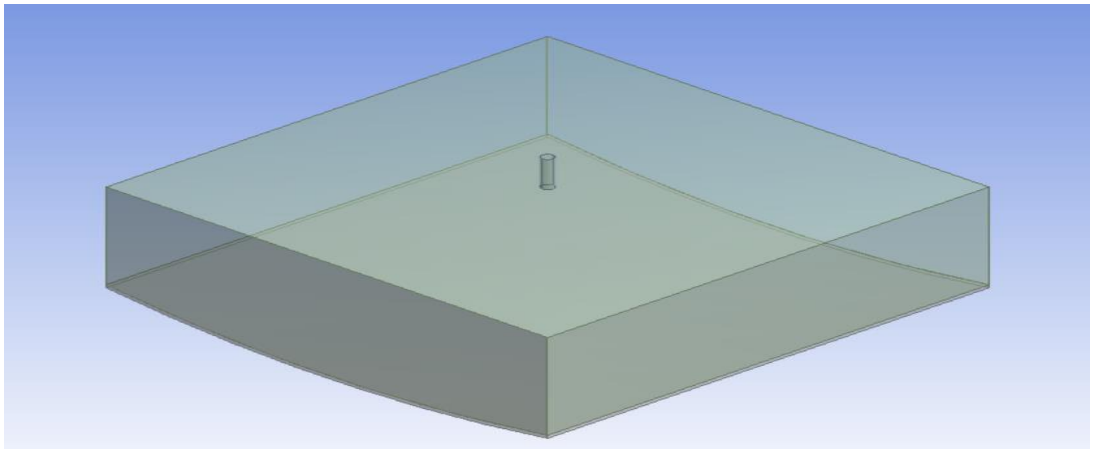

Fig. 3. Geometry in design modeler

In order to use the geometry in ANSYS 19.2, the model was saved in STEP format. The geometry was imported into Design Modeler. The bodies were named nozzle, air, and plate. The bodies were formed as a new part.

There are two methods were used. Multizone meshing was used for air. The sweep method was used for the nozzle and plate. Element size was set at 1mm. Then, named selections were added to define nozzle wall, velocity inlet, pressure inlet, and outlet. The skewness of the mesh is below 0.85. It indicates the mesh quality is good.

2.2 Computational Setup

Named selections were added to define nozzle wall, velocity inlet, pressure inlet, and outlet. The skewness of the mesh is below 0.85. It indicates the mesh quality is good. Energy equation was enabled k-ω model with SST was used. Shear stress transport (SST) turbulence models consist of the advantages of the k-ε and k-ω models, with a blending function that activates the k-ε model in the core region of the flow and shifts to the k-ω model for near-wall region treatment. For material nozzle and air were defined as air in Ansys. The plate was defined as aluminum. The properties of air and aluminum were set as in Table 1 and Table 2.

Table 1
The properties of air

Properties	Value
Density	Ideal gas
Specific Heat	1006.43 J/kg·K
Thermal Conductivity	0.0242 W/m·K
Viscosity	Sutherland
Molecular Weight	28.966 kg/kmol

Table 2
The properties of aluminum

Properties	Value
Density	2719 kg/m^3
Specific Heat	871 J/kg·K
Thermal Conductivity	202.4 W/m·K

2.3 Boundary Conditions

Figure 4 illustrates the boundary condition of the study. Afterward, the temperature of the pressure inlet and outlet was set at 27^{0}C. The velocity of inlet air was set at 20, 22, 24, 26, and 28m/s. The temperature of the inlet air was set at 43, 48, 53, and 58^{0}C. The turbulence specification method of velocity inlet was intensity, 5%, and hydraulic diameter, 0.0025m.

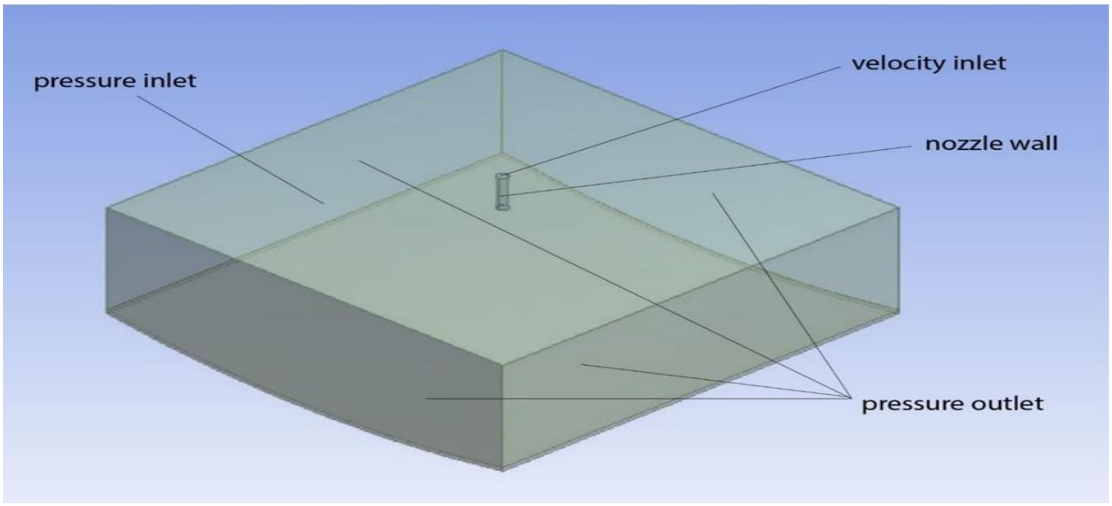

Fig. 4. Boundaries of the geometry

3. Results and discussion

Effect of Reynolds number (*Re*) and hot air temperature on temperature distribution concave plate. In order to study the effect, 5 different velocities of air were used, including 20, 22, 24, 26, and 28m/s. Since the velocity of air has a positive correlation to *Re*, therefore higher velocity indicates higher *Re*. *Re* was calculated by Eq. (1) [20].

$$Re = \frac{\rho v D}{\mu} \tag{1}$$

where ρ, v,D, and μ are air density, jet air velocity, nozzle diameter, and air dynamic viscosity, respective.

The temperature of the concave plate is presented in dimensionless temperature. The dimensionless temperature ($T_{dimensionless}$) at a point is calculated by Eq. (2).

$$T_{dimensionless} = \frac{T_{point} - T_{ambient}}{T_{air} - T_{ambient}} \quad (2)$$

where T_{point}, $T_{ambient}$, T_{air} are local temperature, ambient temperature, and hot air temperature, respectively. Table 3 summarised the temperature on the impingement point.

Table 3
The temperature on the impingement point for R=250mm

Air Temperature, T_{air} (°C)	Temperature on impingement point, T_0 (°C)				
Reynolds Number, Re	2681-2907	2949-3198	3217-3489	3485-3780	3753-4070
43	0.142458	0.143497	0.144592	0.145709	0.146850
48	0.141017	0.141953	0.142942	0.143945	0.144955
53	0.139763	0.140628	0.141547	0.142473	0.143404
58	0.138615	0.138615	0.140292	0.141167	0.142040

Figure 5 to 9 shows the contour plot of $T_{dimensionless}$ on different *Re* with the same scale. The range of *Re* is between 2681 and 3753 with the variation of air velocity from 20m/s to 28m/s. Since the contours use the same scale, it is easy to observe that the $T_{dimensionless}$ is the highest in Figure 1.5 when the *Re* is the highest. When Re=3753, Figure 1.4 shows more reddish on the plot. The $T_{dimensionless}$ on the impingement point is 0.142040 and the minimum $T_{dimensionless}$ is 0.129511 at the four corners. The $T_{dimensionless}$ decreases when the *Re* decrease from 3753 to 2681. When Re=2681, Figure 1.8 shows more bluish on the plot. The $T_{dimensionless}$ on impingement, the point is 0.135189, and the minimum $T_{dimensionless}$ is 0.128556451 at the four corners.

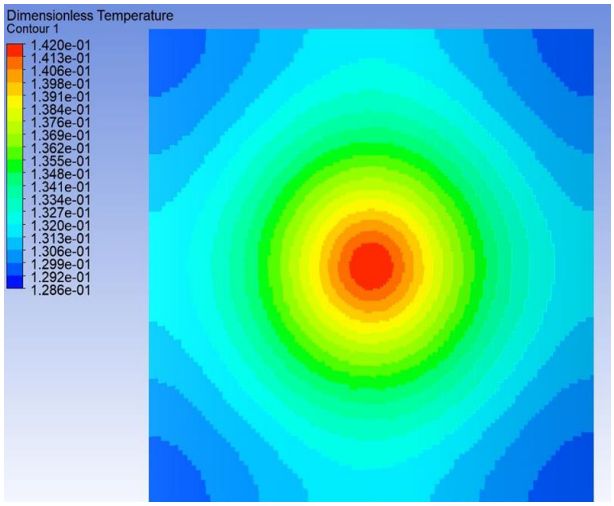

Fig. 5. Temperature contour of the concave plate for 250mm, 58°C, 28m/s

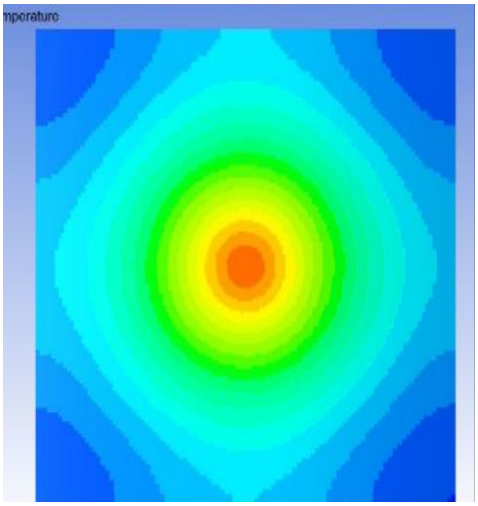

Fig. 6. Temperature contour of the concave plate for 250mm, 58°C, 26m/s

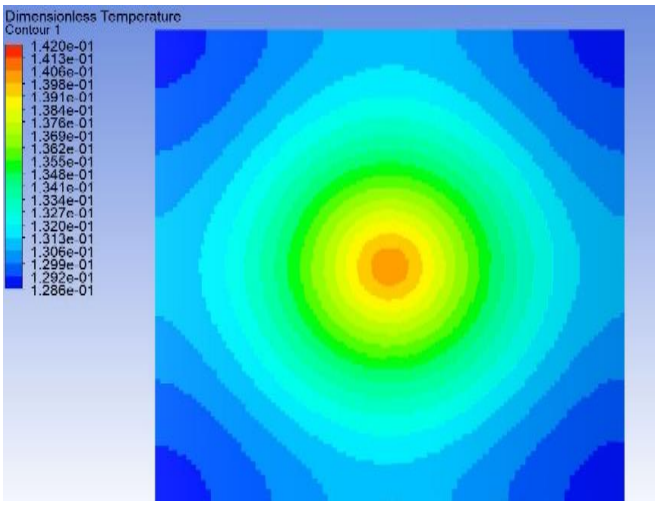

Fig. 7. Temperature contour of the concave plate for 250mm, 58°C, 24m/s

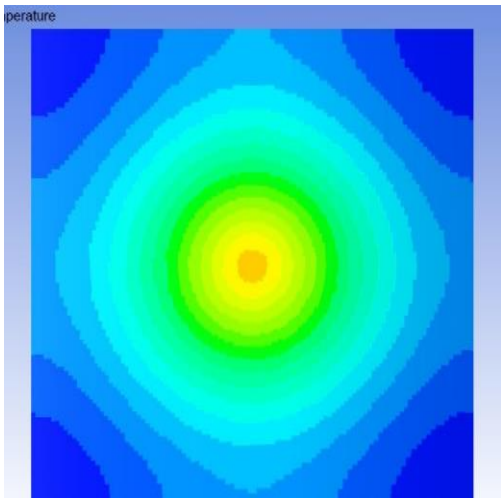

Fig. 8. Temperature contour of the concave plate for 250mm, 58°C, 22m/s

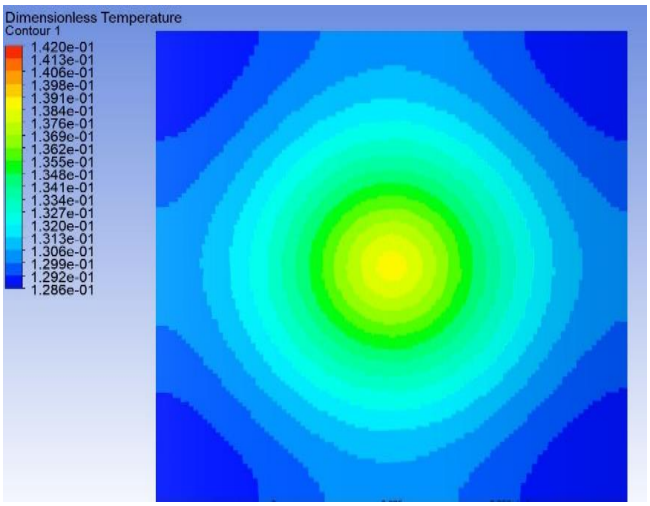

Fig. 9. Temperature contour of the concave plate for 250mm, 58°C, 20m/s

Based on Figure 10 and 11, *Re* and $T_{dimensionless}$ have a positive correlation. The $T_{dimensionless}$ increases linearly with *Re*. The difference is around 0.0008 with the increase of 268 in *Re* or 2 m/s in air velocity. The increase in velocity increases the Reynold number of the flow. Volumetric flow if the air is higher at high velocity, more air is involved in the heat transfer. The higher the *Re*, the higher the Nusselt number, indicating more heat is transferred. Therefore, the $T_{dimensionless}$ of the concave plate increases when *Re* increases.

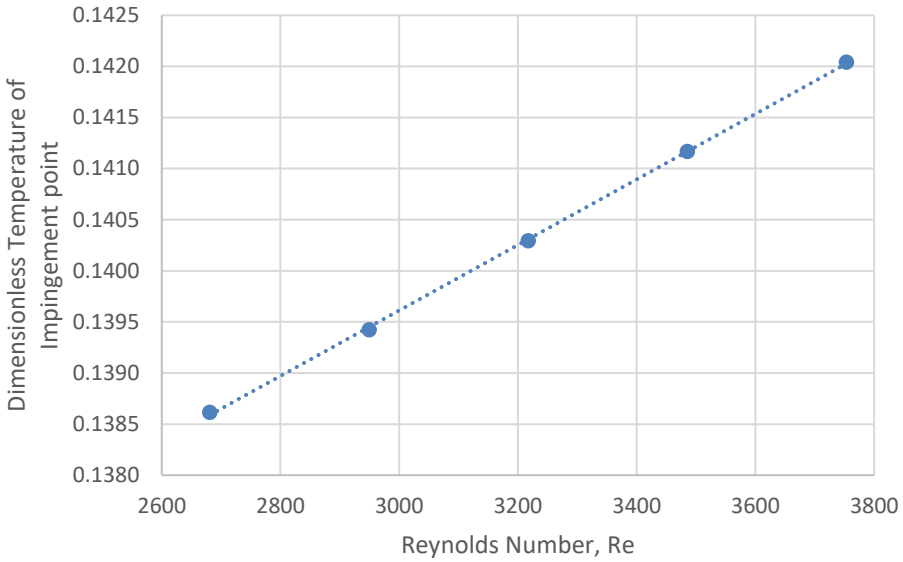

Fig. 10. Graph of maximum $T_{dimensionless}$ of impingement point against *Re*

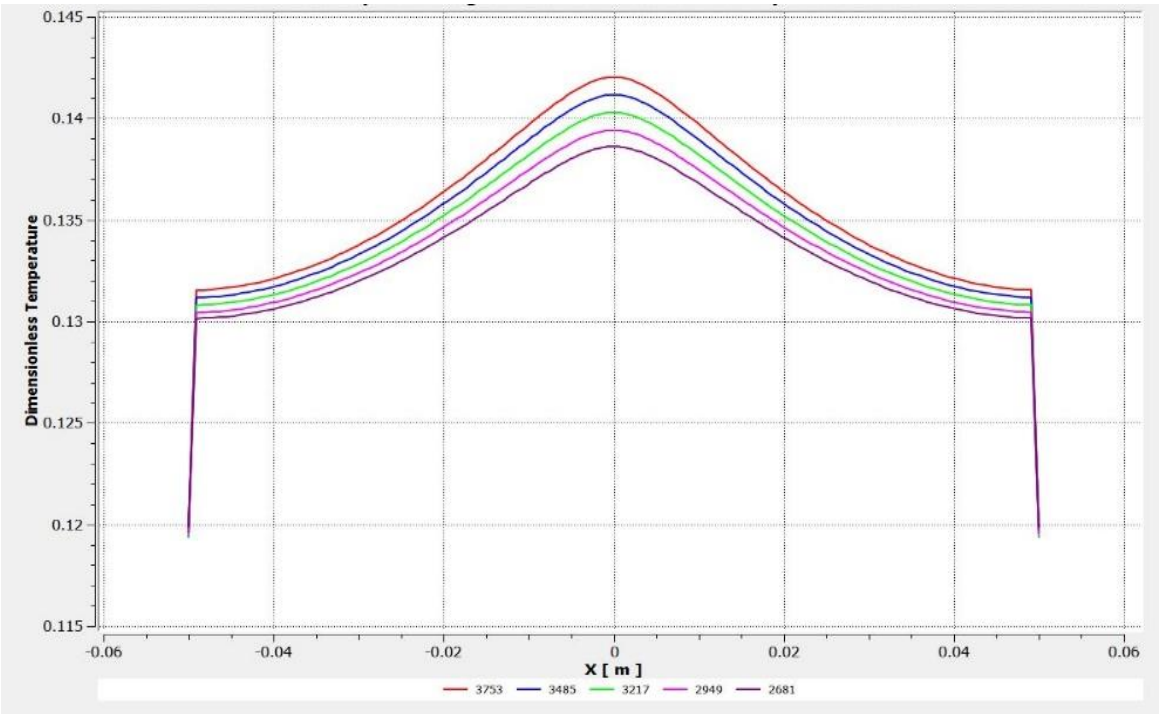

Fig. 11. Graph of $T_{dimensionless}$ against X-axis with different *Re*

Figure 12 shows the velocity magnitude contour plot on XY plane under the set of 28m/s air velocity, 58°C air temperature, 300mm of curvature radius. The air is flowing at its maximum velocity along with the pipe nozzle. When it reaches the opening of the nozzle, the air diffuses and the velocity decreases when it flows towards the concave plate.

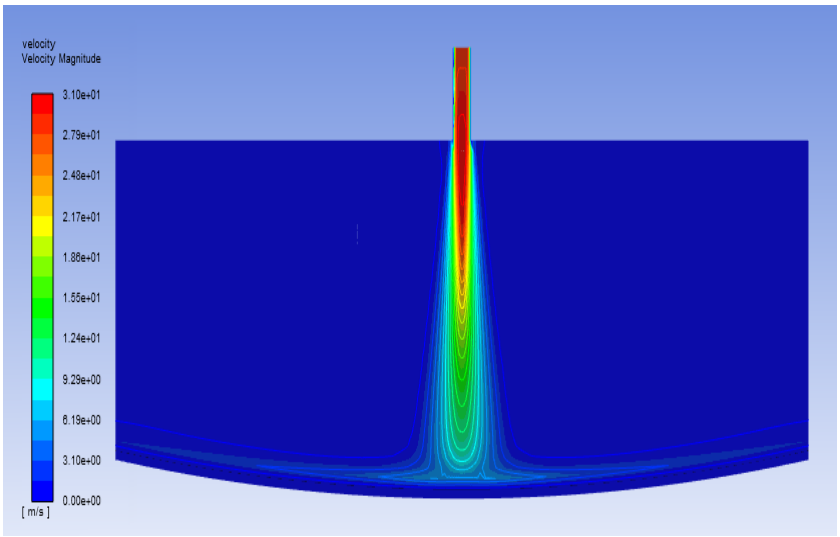

Fig. 12. Velocity magnitude contour plot on XY plane

Figure 13 to 16 shows the contour plot of $T_{dimensionless}$ on different hot air temperatures with the same scale (0.1295-0.1469). The temperature of air varies from 43°C to 58°C. From the contour plots, lower temperature results in higher$T_{dimensionless}$. The plot is more reddish at 43°C. In comparison, the $T_{dimensionless}$ on impingement, the point is 0.146850 when the air temperature is 43°C, 0.144955 when the air temperature is 48°C, 0.143404 when the air temperature is 53°C and lastly it decreases to 0.142040 when the air temperature is 58°C.

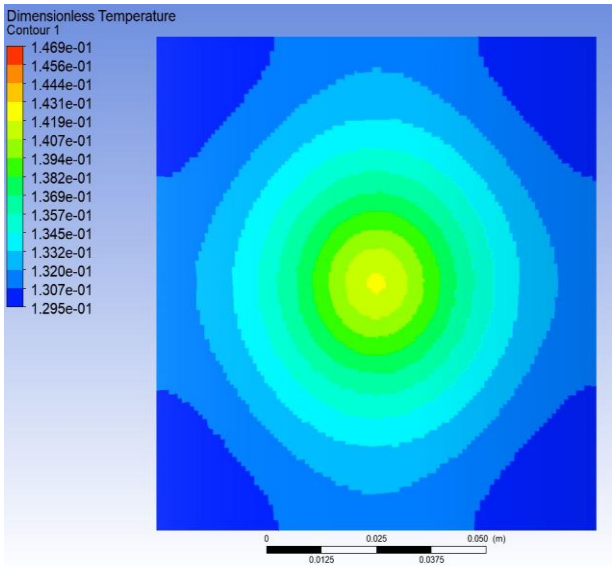

Fig. 13. Temperature contour of the concave plate for 250mm, 58°C, 28m/s

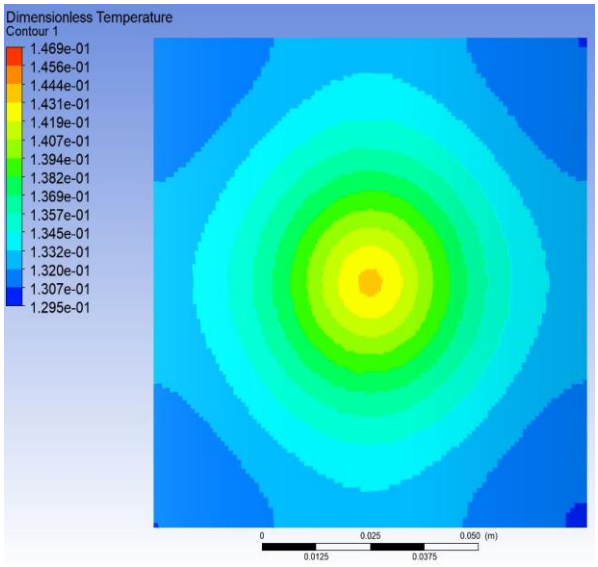

Fig. 14. Temperature contour of the concave plate for 250mm, 53°C, 28m/s

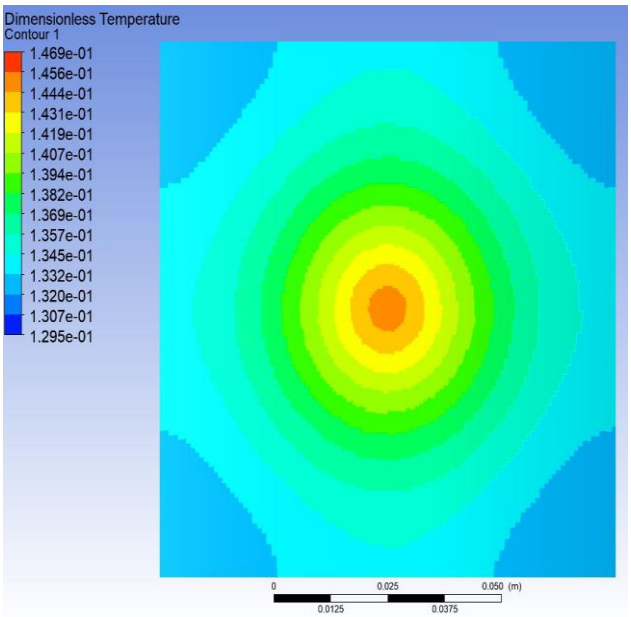

Fig. 15. Temperature contour of the concave plate for 250mm, 48°C, 28m/s

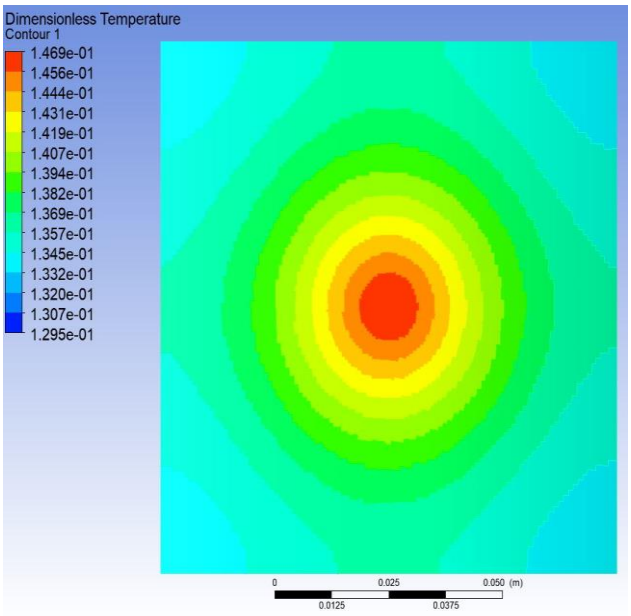

Fig. 16. Temperature contour of the concave plate for 250mm, 43°C, 28m/s

The trend can be observed from Figure 17 and 18 as well. Figure 17 shows that the $T_{dimensionless}$ decreases with increasing air temperature. The decrement is not linear, it decreases from 0.001895 to 0.001551 and lastly 0.001364.

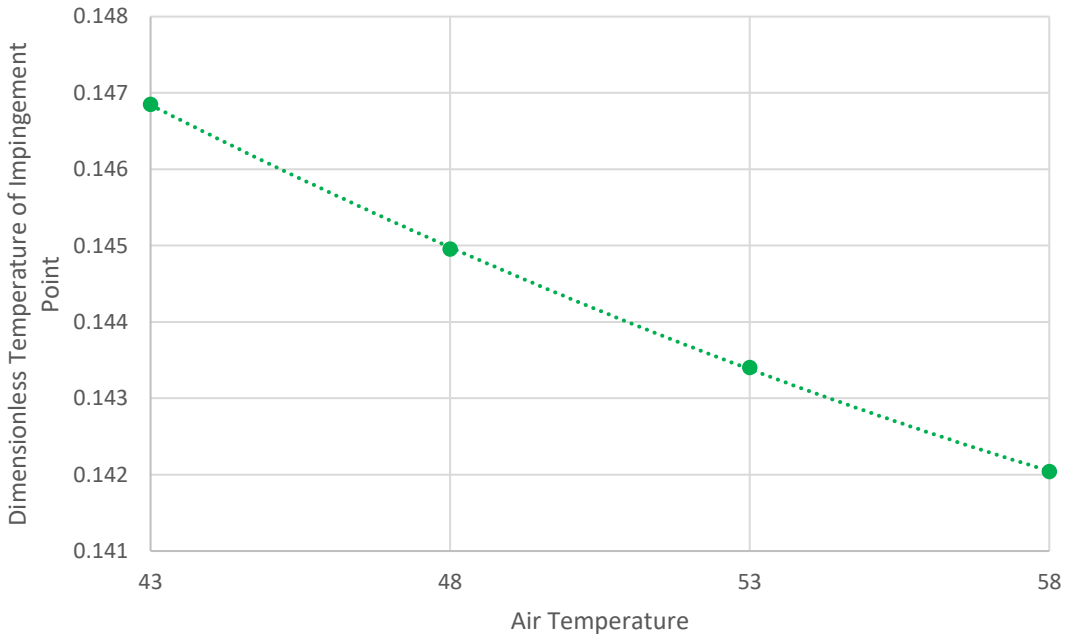

Fig. 17. Graph of maximum $T_{dimensionless}$ of impingement point against T_{air}

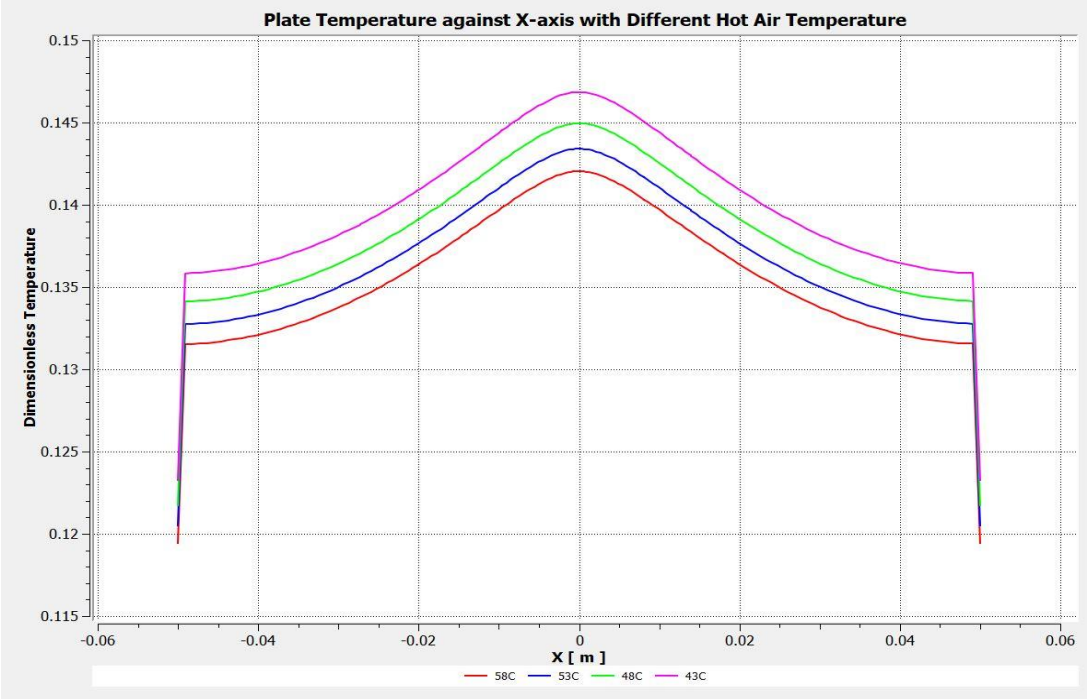

Fig. 18. Graph of $T_{dimensionless}$ against X-axis with different T_{air} for *Re* from 3753 to 4070

$T_{dimensionless}$ can measure the performance of the system. The performance of the system at lower air temperatures is better. It is because less heat is transferred to the ambient. The temperature difference between hot air and ambient air is one of the factors affecting convective heat transfer. The formula of convection heat transfer, Eq. (3),

$Q = h_{convection}\ A\Delta T$	(3)

shows that the higher the temperature difference, ΔT, the higher the heat transfer. Hence, when the impingement air temperature is higher, more heat is transferred to ambient air through convection. Although the temperature of the concave plate is higher, the $T_{dimensionless}$ shows that the performance of the system is lower. Some of the heat is transferred to the ambient air instead of the concave plate.

Effect of concave radius on the temperature distribution concave plate. Figure 19 to 22 shows the contour plot of $T_{dimensionless}$ on different curvature radius with the same scale (0.1268-0.1423). The curvature radius of the concave plate varies from 150mm to 300mm. From the contour plots, a higher curvature radius results in a higher$T_{dimensionless}$. The red spot at the middle is the largest in Figure 19 when the curvature radius is 300mm.

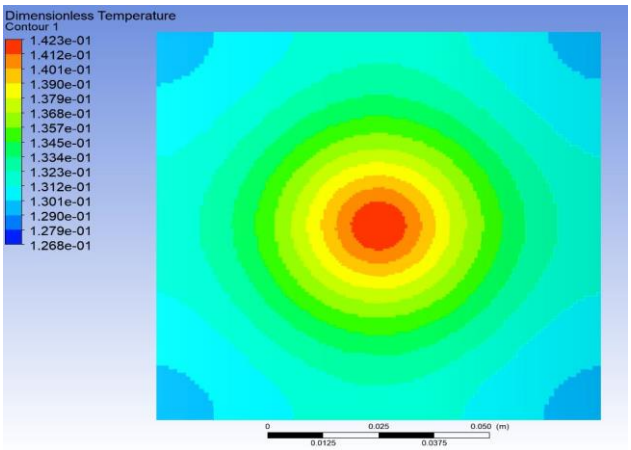

Fig. 19. Temperature contour of the concave plate for 300mm, 58°C, 28m/s

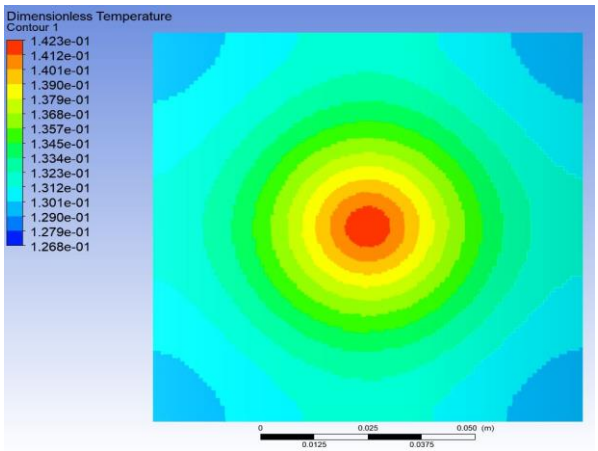

Fig. 20. Temperature contour of the concave plate for 250mm, 58°C, 28m/s

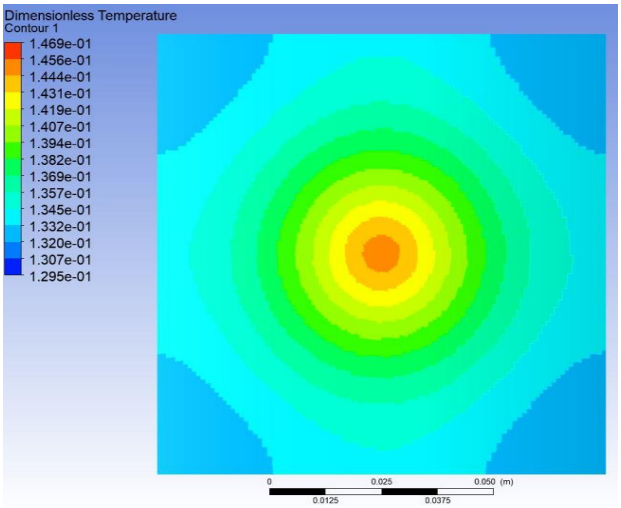

Fig. 21. Temperature contour of the concave plate for 200mm, 58°C, 28m/s

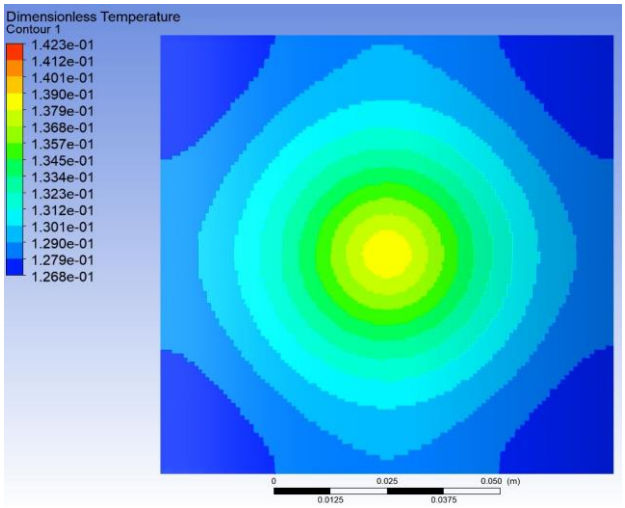

Fig. 22. Temperature contour of the concave plate for 150mm, 58°C, 28m/s

From Figure 23 and Figure 24, curvature radius has a positive effect to the $T_{dimensionless}$ of the plate. The temperature increases from 0.138747 to 0.142316 when the curvature radius increases from 150mm to 300mm.

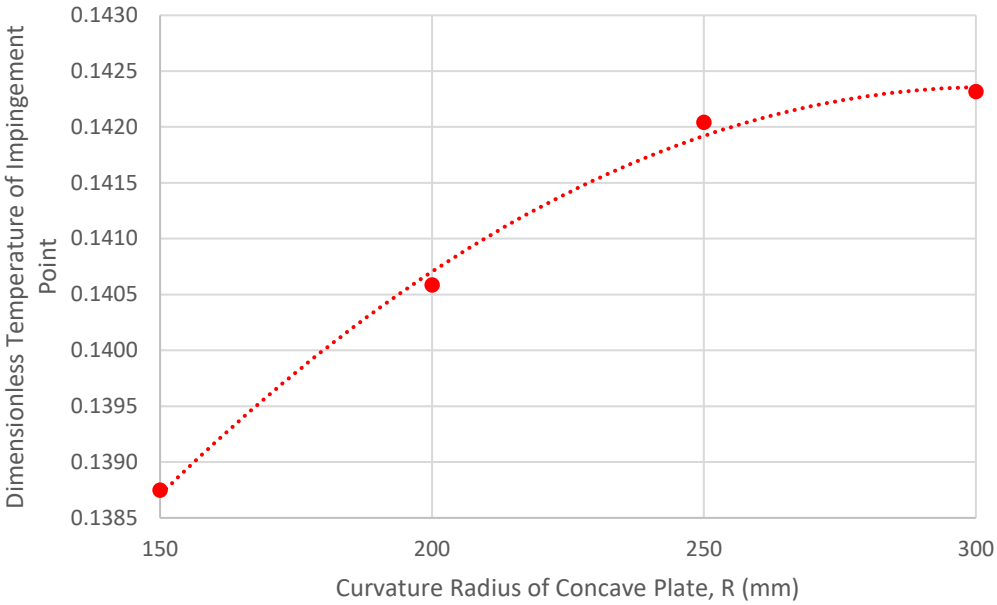

Fig. 23. Graph of Maximum $T_{dimensionless}$ of Impingement Point against Curvature Radius

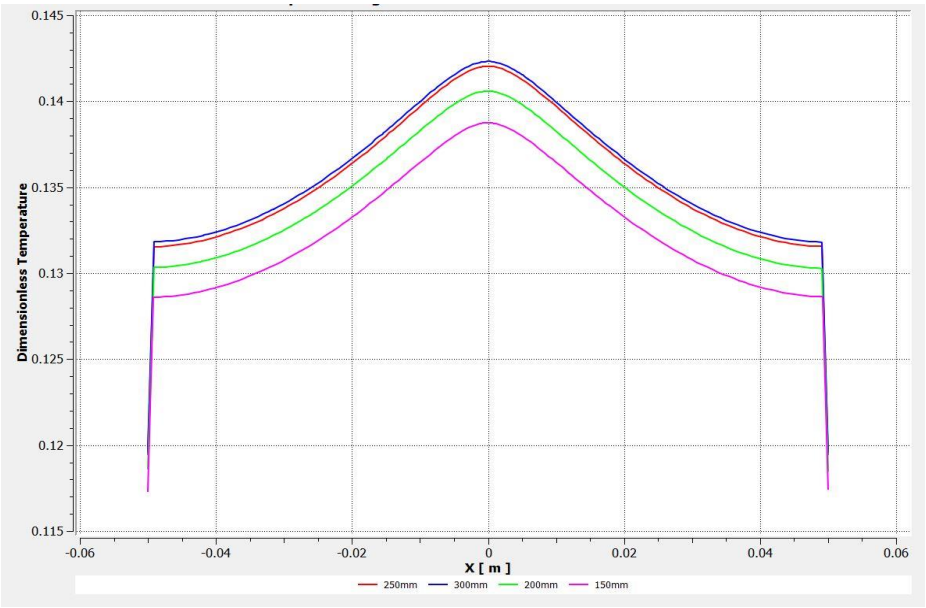

Fig. 24. Graph of $T_{dimensionless}$ against X-axis with different Curvature Radius

However, the increment is not uniform. The increment decreases even though the increment of the curvature radius is the same. Table 4 shows the curvature radius and area of the surface.

Table 4
The curvature radius and area of the surface

Curvature Radius, R (mm)	Area of the surface, A (cm^2)
150	101.951
200	101.072
250	100.679
300	100.469

The result is caused by the area of the plate. When the radius curvature increases, the area of the plate decreases. The trend of the area is shown in Figure 25, it is the inverse of the graph of $T_{dimensionless}$ of impingement point against curvature radius. The increase in the area promotes the dissipation of heat to ambient air. It can be further proven by the negative heat flux shown in Figure 26. The side region of the plate transfers heat to the ambient air. Increasing curvature radius causes the region of negative heat flux to decrease. Hence, the $T_{dimensionless}$ increases with increasing curvature radius. In other words, the thermal performance is better on a higher curvature radius.

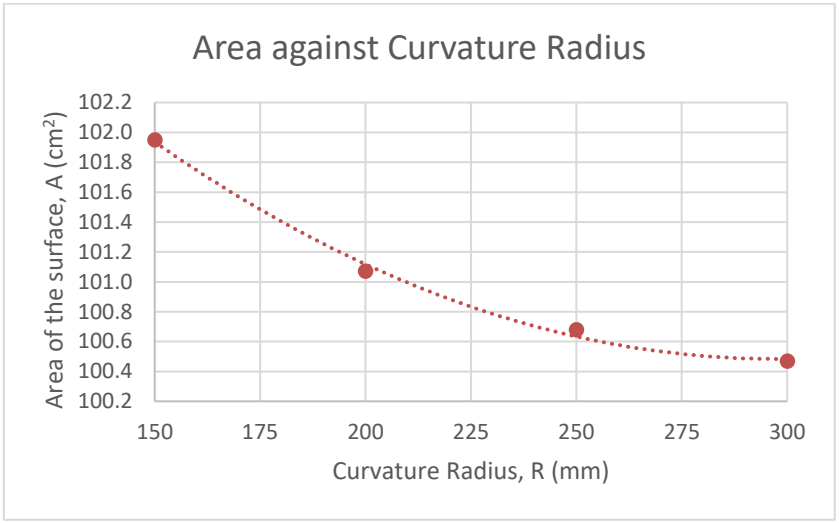

Fig. 25. Graph of Surface Area against Curvature Radius

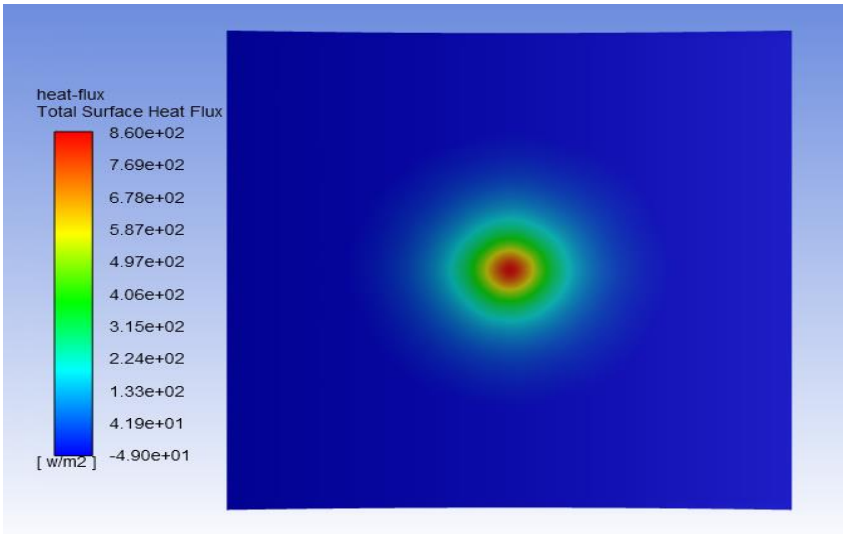

Fig. 26. Heat Flux Contour Plot of Concave Plate

4. Conclusions

A total of 80 sets of the simulation was completed to study the effect of *Re* of impingement flow, hot air temperature, and curvature radius on temperature distribution of concave plate. A few conclusions can be made as below

i. The validation was successfully done by using the correlation between Nusselt number on impingement point and *Re* developed by Mohanty and Tawfek (1993) with a percentage error of 0.09% to 6.11%.
ii. The $T_{dimensionless}$ of concave plate increases when *Re* increases and hot air temperature decreases. The highest $T_{dimensionless}$ recorded is 0.147125 under the set of 300mm curvature radius, air temperature of 43°C, *Re* of 4070.
iii. The $T_{dimensionless}$ of the plate decreases with the curvature radius decreases due to the increase of heat dissipation. The $T_{dimensionless}$ increases from 0.138747 to 0.142316 when the curvature radius increases from 150mm to 300mm.

Acknowledgement
This research was funded by a fundamental research grant scheme (FRGS) from the Ministry of Higher Education of Malaysia (FRGS/1/2018/TK09/USM/03/3).

References

[1] Ismail, Mohd Azmi, and Jian Wang. "Effect of nozzle rotation angles and sizes on thermal characteristic of swirl anti-icing." *Journal of Mechanical Science and Technology* 32, no. 9 (2018): 4485-4493. https://doi.org/10.1007/s12206-018-0845-x
[2] Ramamurthy, Subramaniam, Theo G. Keith, Kenneth J. De Witt, James C. Putt, Charles A. Mailing, and Kevin L. Leffel. "Numerical modeling of an advanced pneumatic impulse ice protection system for aircraft." *Journal of Aircraft* 29, no. 6 (1992): 1057-1063. https://doi.org/10.2514/3.46284
[3] Egbert, Robert I., Robert L. Schrag, Walter D. Bernhart, Glen W. Zumwalt, and Thomas J. Kendrew. "An investigation of power line de-icing by electro-impulse methods." *IEEE transactions on power delivery* 4, no. 3 (1989): 1855-1861. https://doi.org/10.1109/61.32682
[4] Labeas, George N., Ioannis D. Diamantakos, and Milan M. Sunaric. "Simulation of the electroimpulse de-icing process of aircraft wings." *Journal of Aircraft* 43, no. 6 (2006): 1876-1885. https://doi.org/10.2514/1.21321
[5] Ross, J. F., and J. T. Connolly. "Contrasting requirements for type II de/anti-icing fluids." *Journal of Aircraft* 30, no. 1 (1993): 10-13. https://doi.org/10.2514/3.56875
[6] Brown, J. M., Srinivasan Raghunathan, J. K. Watterson, A. J. Linton, and D. Riordon. "Heat transfer correlation for anti-icing systems." *Journal of aircraft* 39, no. 1 (2002): 65-70. https://doi.org/10.2514/2.2896
[7] Khai, Lee Chern, Mohd Azmi Ismail, Qummare Azam, and Nurul Musfirah Mazlan. "Experimental study on aerodynamic performance of nacelle lip-skin bias flow." *Journal of Mechanical Science and Technology* 34, no. 4 (2020): 1613-1621. https://doi.org/10.1007/s12206-020-0323-0
[8] Cao, Yihua, Junsen Huang, and Jun Yin. "Numerical simulation of three-dimensional ice accretion on an aircraft wing." *International Journal of Heat and Mass Transfer* 92 (2016): 34-54. https://doi.org/10.1016/j.ijheatmasstransfer.2015.08.027
[9] Potapczuk, Mark G. "Aircraft icing research at NASA Glenn research center." *Journal of Aerospace Engineering* 26, no. 2 (2013): 260-276. https://doi.org/10.1061/(ASCE)AS.1943-5525.0000322
[10] Nagappan, Nikisha Maria. "Numerical modeling of anti-icing using an array of heated synthetic jets." (2013).
[11] Sreedharan, C., Q. H. Nagpurwala, and S. Subbaramu. "Effect of Hot Air Jets from a Piccolo Tube in Aircraft Wing Anti-Icing Unit." *MSRUAS-SASTech Journal* 13, no. 2 (2014): 2-5.
[12] Saeed, Farooq. "State-of-the-art aircraft icing and anti-icing simulation." *ARA Journal* 2000, no. 25-26 (2003): 106-113.
[13] Thomas, Scott K., Robert P. Cassoni, and Charles D. MacArthur. "Aircraft anti-icing and de-icing techniques and modeling." *Journal of aircraft* 33, no. 5 (1996): 841-854. https://doi.org/10.2514/3.47027
[14] Lynch, Frank T., and Abdollah Khodadoust. "Effects of ice accretions on aircraft aerodynamics." *Progress in Aerospace Sciences* 37, no. 8 (2001): 669-767. https://doi.org/10.1016/S0376-0421(01)00018-5
[15] Hann, Richard, Adriana Enache, Mikkel Cornelius Nielsen, Bård Nagy Stovner, Jeroen van Beeck, Tor Arne Johansen, and Kasper Trolle Borup. "Experimental Heat Loads for Electrothermal Anti-Icing and De-Icing on UAVs." *Aerospace* 8, no. 3 (2021): 83. https://doi.org/10.3390/aerospace8030083
[16] S. Aerospace. "Ice, Rain, Fog, and Frost Protection." An SAE International Group, USA, 2016.
[17] Seyedein, S. H., M. Hasan, and A. S. Mujumdar. "Modelling of a single confined turbulent slot jet impingement using various k—ϵ turbulence models." *Applied Mathematical Modelling* 18, no. 10 (1994): 526-537. https://doi.org/10.1016/0307-904X(94)90138-4

[18] Shi, Yuling, M. B. Ray, and A. S. Mujumdar. "Computational study of impingement heat transfer under a turbulent slot jet." *Industrial & Engineering Chemistry Research* 41, no. 18 (2002): 4643-4651. https://doi.org/10.1021/ie020120a

[19] Azmi, Husin, Mohd Zulkifly Abdullah, and Mohd A. Ismail. "Numerical and experimental investigations of speaker-driven synthetic jet actuator for electronics cooling applications." *Heat Transfer Research* 50, no. 14 (2019): 1369–1381. https://doi.org/10.1615/HeatTransRes.2019026060

[20] Ismail, Mohd Azmi, R. H. Z. Yu, M. I. Ramdan, and K. H. Yu. "EXPERIMENTAL STUDY OF SYNTHETIC JET PERFORMANCE IN COMBINED CONVECTION HEAT TRANSFER." *Heat Transfer Research* 52, no. 1 (2021). https://doi.org/10.1615/HeatTransRes.2020033493

[21] Akaje, Wasiu, and B. I. Olajuwon. "Impacts of Nonlinear thermal radiation on a stagnation point of an aligned MHD Casson nanofluid flow with Thompson and Troian slip boundary condition." *Journal of Advanced Research in Experimental Fluid Mechanics and Heat Transfer* 6, no. 1 (2021): 1-15.